Linear Gyrokinetic Analyses of ITG Modes and Zonal Flows in LHD with High Ion Temperature

Masanori NUNAMI$^{1)}$, Tomo-Hiko WATANABE$^{1,2)}$, Hideo SUGAMA$^{1,2)}$ and Kenji TANAKA$^{1)}$

$^{1)}$*National Institute for Fusion Science, Toki 509-5292, Japan*

$^{2)}$*The Graduate University for Advanced Studies (SOKENDAI), Toki 509-5292, Japan*

(Received 16 September 2010 / Accepted 15 November 2010)

Ion temperature (T_i) gradient modes (ITG modes) and zonal flows for high T_i discharges in the Large Helical Device (LHD) are investigated by linear gyrokinetic Vlasov simulation. In recent LHD experiments, high T_i plasmas are generated by neutral beam injection, and spatial profiles of density fluctuations are measured by phase contrast imaging (PCI) [K. Tanaka *et al.*, Plasma Fusion Res. **5**, S2053 (2010)]. The observed fluctuations most likely propagate in the direction of the ion diamagnetic rotation in the plasma frame, and their amplitudes increase with the growth of the temperature gradient. The results show the characteristics of ITG turbulence. To investigate the ITG modes and zonal flows in the experiment, linear gyrokinetic simulations were performed in the corresponding equilibria with different T_i profiles by using the GKV-X code [M. Nunami *et al.*, Plasma Fusion Res. **5**, 016 (2010)]. The simulation results predict unstable regions for the ITG modes in radial, wavenumber, and phase velocity spaces, in agreement with the PCI measurements. Thus, the fluctuations observed in the experiment are attributed to ITG instability. The responses of the zonal flows show clear contrasts in different field spectra that depend on the T_i profile and the radial position. In addition to the dependence on the field spectra, the zonal flow residual levels are enhanced by increasing the radial wavenumber as theoretically predicted.

© 2011 The Japan Society of Plasma Science and Nuclear Fusion Research

Keywords: gyrokinetic simulation, LHD, ITG mode, zonal flow, high ion temperature

DOI: 10.1585/pfr.6.1403001

1. Introduction

Achieving high ion temperature (T_i) in confinement plasmas is one of the keys to realize a magnetic fusion reactor, and anomalous transport of the plasmas which can be driven by drift wave plasma turbulence [1] is a critical issue in fusion research. In recent Large Helical Device (LHD) [2] experiments, high-T_i discharges ($T_\mathrm{i} \sim 5.6\,\mathrm{keV}$) have been achieved by high-power neutral beam injection [3]. For better understanding of transport physics in such experiments, quantitative comparisons should be conducted between the experimental observations and computational simulations including zonal flows which play a significant role in regulating turbulent transport in toroidal plasmas [4–6]. In fact, nonlinear gyrokinetic simulations have shown that ion temperature gradient (ITG) turbulent transport in LHD plasma is reduced when the zonal flow generation is enhanced in the inward-shifted LHD configuration [7, 8].

Figures 1-(a) and (d) show the radial profiles of the density and the ion and electron temperatures obtained from the LHD high-T_i discharge of shot number 88343 [9, 10] in the low-T_i ($t = 1.833\,\mathrm{s}$) and high-T_i phases ($t = 2.233\,\mathrm{s}$), respectively. The spatial distributions of the density fluctuations were also measured by two-dimensional phase contrast imaging (2D-PCI) [11]. Figures 1-(b) and (e) show the distributions of the density fluctuations in k_θ-ρ space, and Figs. 1-(c) and (f) show them in v_lab-ρ space. Here k_θ is the poloidal wavenumber, v_lab is the phase velocity in the laboratory frame, and ρ is the normalized minor radius defined below Eq. (3) in the next section. From the results, the positions in k_θ-ρ space where the fluctuation increases are obtained as

$$\rho^\mathrm{exp}_\mathrm{peak} \sim \begin{cases} 0.8\text{ - }1.0 \\ 0.6\text{ - }0.8 \end{cases}, \quad \text{and} \quad (k_\theta\rho_\mathrm{ti})^\mathrm{exp}_\mathrm{peak} \sim \begin{cases} 0.26 & \text{for low-}T_\mathrm{i}\text{ phase} \\ 0.45 & \text{for high-}T_\mathrm{i}\text{ phase} \end{cases}, \tag{1}$$

where the ion thermal gyroradius is defined as $\rho_\mathrm{ti} \equiv v_\mathrm{ti}/\Omega_\mathrm{i}$, with the ion gyro frequency $\Omega_\mathrm{i} = eB/m_\mathrm{i}c$ and the ion thermal speed $v_\mathrm{ti} = \sqrt{T_\mathrm{i}/m_\mathrm{i}}$ which is obtained from the T_i profiles in the experiment. For example, $\rho_\mathrm{ti} \sim 1.0 \times 10^{-3}\,\mathrm{m}$ at $\rho \sim 0.9$ in the low-T_i phase, and $\rho_\mathrm{ti} \sim 1.8 \times 10^{-3}\,\mathrm{m}$ at $\rho \sim 0.7$ in the high-T_i phase. The phase velocities of the fluctuations in the $\boldsymbol{E} \times \boldsymbol{B}$ rotating frame (plasma frame), $v^\mathrm{exp}_\mathrm{ph} = v_\mathrm{lab} - v_{E\times B}$, are given by

$$v^\mathrm{exp}_\mathrm{ph} \sim \begin{cases} -1.7 \times 10^3\,\mathrm{m/s} \\ \quad \text{at } \rho = 0.98 \quad \text{for low-}T_\mathrm{i}\text{ phase} \\ -3.4 \times 10^3\,\mathrm{m/s} \\ \quad \text{at } \rho = 0.80 \quad \text{for high-}T_\mathrm{i}\text{ phase} \end{cases}, \tag{2}$$

where the observed velocities in the laboratory frame are $v_\mathrm{lab} \sim -1.1 \times 10^3\,\mathrm{m/s}$ (low-T_i) and $v_\mathrm{lab} \sim -3.9 \times 10^3\,\mathrm{m/s}$

---

author's e-mail: nunami.masanori@nifs.ac.jp

© 2011 The Japan Society of Plasma Science and Nuclear Fusion Research

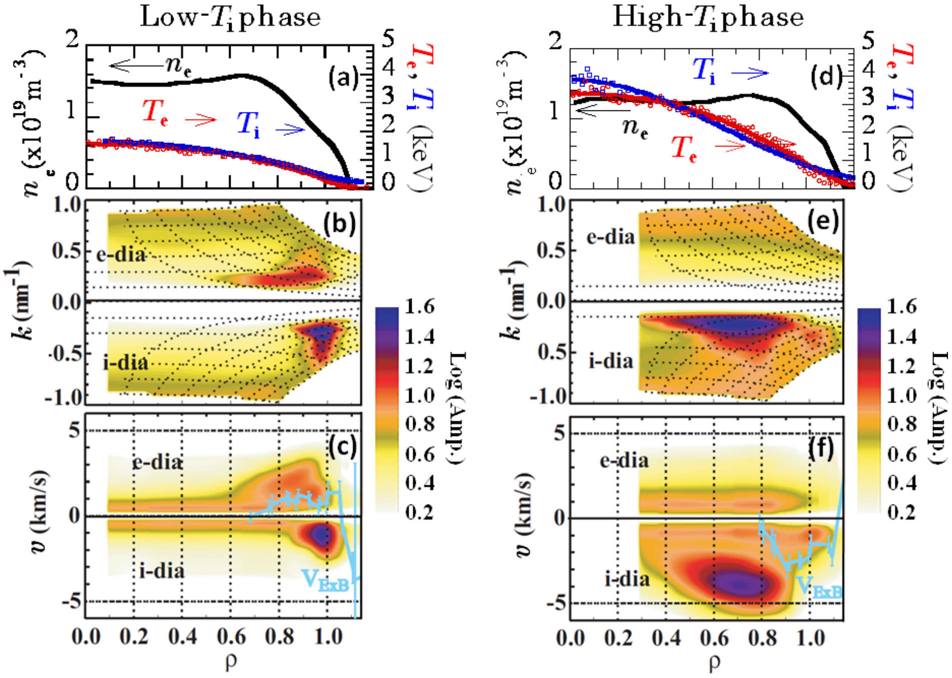

Fig. 1 Radial profiles of electron density, ion temperature, and electron temperature ((a) and (d)), the density fluctuations in wavenumber space ((b) and (e)), and phase velocity space ((c) and (f)), for low-T_i ((a), (b), and (c)) and high-T_i ((d), (e), and (f)) phases. Light blue curves in (c) and (f) represent the $\boldsymbol{E} \times \boldsymbol{B}$ poloidal rotation velocities $v_{E\times B}$ in the laboratory frame. Here, "i-dia" and "e-dia" indicate the directions of ion diamagnetic and electron diamagnetic rotation in the laboratory frame, respectively. The plots are cited from Ref. [10].

(high-T_i), and the poloidal $\boldsymbol{E}\times\boldsymbol{B}$ rotational velocities $v_{E\times B}$, which are obtained by charge exchange spectroscopy and plotted in Figs. 1-(c) and (f), are $v_{E\times B} \sim +0.6 \times 10^3$ m/s (low-T_i) and $v_{E\times B} \sim -0.5 \times 10^3$ m/s (high-T_i). Here, the minus sign of the velocities represents the direction of the ion diamagnetic rotation. Thus, the large-amplitude fluctuations observed in the plasma frame propagate in the direction of the ion diamagnetic rotation, which is one of the features of ITG modes, and the velocity in the high-T_i phase is greater than that in the low-T_i phase. Therefore, the experimentally observed fluctuations are considered to be driven by ITG modes.

In this study, to investigate the characteristics of the experimentally observed density fluctuations, we perform linear gyrokinetic simulations in the equilibrium magnetic field corresponding to the LHD discharge by using the GKV-X code [12] and compare the simulation results with the experimental observations. This paper is organized as follows. In Sec. 2, we briefly describe GKV-X and the basic equations employed in the calculation. In Sec. 3, we show the linear simulation results for the ITG modes and the zonal flow responses in the LHD experiment with different T_i profiles and compare the results for the ITG modes obtained from the simulations and the fluctuation measurements. Finally, we present our conclusions in Sec. 4.

2. GKV-X Code

GKV-X is a gyrokinetic Vlasov flux-tube code that can handle the three-dimensional magnetic field corresponding to experiments in non-axisymmetric systems such as the LHD. GKV-X incorporates full geometrical information on the non-axisymmetric confinement field, as well as the Fourier components of the field obtained from the MHD equilibrium code VMEC [13] through coordinate transformation into Boozer coordinates [14], $\{\rho, \theta_\mathrm{B}, \zeta_\mathrm{B}\}$. The magnetic field strength is represented in the coordinate system as

$$\begin{aligned} B \;=\; & \sum_{n=0}^{n_\mathrm{max}} B_{0n}(\rho)\cos n\zeta_\mathrm{B} \\ & + \sum_{m=1}^{m_\mathrm{max}} \sum_{n=-n_\mathrm{max}}^{n_\mathrm{max}} B_{mn}(\rho)\cos(m\theta_\mathrm{B} - n\zeta_\mathrm{B}), \end{aligned} \tag{3}$$

where the flux labeling index (or normalized minor radius) is defined by $\rho \equiv \sqrt{\Psi/\Psi_a}$, with the toroidal magnetic flux $\Psi = B_\mathrm{ax} r^2/2$ at the minor radius r and Ψ_a at the last closed surface ($r = a$). Here, B_ax is the field strength at the magnetic axis, $B_{mn}(\rho)$ is the Fourier component of the magnetic field with the poloidal and toroidal mode numbers (m, n), and the maximum mode numbers for poloidal and toroidal directions used in the VMEC calculation are denoted by m_max and n_max, respectively. From the information of the flux surface shapes obtained using the VMEC code, the metric tensor can be obtained. In addition, the Jacobian on the flux surface is also obtained from the covariant components of the magnetic field, B_θ, B_ζ, in Boozer coordinates,

$$\begin{aligned}\sqrt{g_{\mathrm{B}}} &= (\nabla\rho\times\nabla\theta_{\mathrm{B}}\cdot\nabla\zeta_{\mathrm{B}})^{-1}\\ &= \frac{\Psi'}{B^2}\left(B_\zeta + q^{-1}(\rho)B_\theta\right),\end{aligned} \tag{4}$$

where q is the safety factor, and the prime symbol represents the derivative with respect to the flux label ρ, i.e., $A' = \mathrm{d}A/\mathrm{d}\rho$. In the code, we used the local flux-tube model [15] with the field-aligned coordinates $\{x, y, z\} = \{r - r_0, (r_0/q_0)\left[q(\rho)\theta_{\mathrm{B}} - \zeta_{\mathrm{B}}\right], \theta_{\mathrm{B}}\}$ and the safety factor q_0 at the minor radius $r = r_0$ defined by the toroidal magnetic flux $\Psi(r_0) = B_{\mathrm{ax}}r_0^2/2$. Then, we regard the coordinate $z = \theta_{\mathrm{B}}$ as a coordinate along the field line labeled by $\alpha = \zeta_{\mathrm{B}} - q_0\theta_{\mathrm{B}} = \text{constant}$.

GKV-X solves the electrostatic gyrokinetic equation for the perturbed ion gyrocenter distribution function δf [16, 17],

$$\begin{aligned}&\left(\frac{\partial}{\partial t} + v_\parallel\boldsymbol{b}\cdot\nabla + \frac{c}{B}\boldsymbol{b}\times\nabla\Phi\cdot\nabla - \frac{\mu}{m_{\mathrm{i}}}\boldsymbol{b}\cdot\nabla B\frac{\partial}{\partial v_\parallel} + \boldsymbol{v}_{\mathrm{d}}\cdot\nabla\right)\delta f\\ &\quad = (\boldsymbol{v}_* - \boldsymbol{v}_{\mathrm{d}} - v_\parallel\boldsymbol{b})\cdot\frac{e\nabla\Phi}{T_{\mathrm{i}}}F_{\mathrm{M}} + C(\delta f),\end{aligned} \tag{5}$$

where the velocity-space coordinates $v_\parallel$ and $\mu = m_{\mathrm{i}}v_\perp^2/2B$ represent the parallel velocity and magnetic moment, respectively. The Maxwellian distribution with temperature T_{i} is denoted by F_{M}, the collision term is written as $C(\delta f)$, and $\boldsymbol{b} = \boldsymbol{B}/B$ is the unit vector parallel to the magnetic field. The magnetic and diamagnetic drift velocities are defined by $\boldsymbol{v}_{\mathrm{d}} = (c/eB)\boldsymbol{b}\times(\mu\nabla B + m_{\mathrm{i}}v_\parallel^2\boldsymbol{b}\cdot\nabla\boldsymbol{b})$ and $\boldsymbol{v}_* = (cT_{\mathrm{i}}/eB)\boldsymbol{b}\times[\nabla\ln n + (m_{\mathrm{i}}v^2/2T_{\mathrm{i}} - 3/2)\nabla\ln T_{\mathrm{i}}]$, respectively. In the wavenumber space (k_x, k_y), the gyro-phase-averaged electrostatic potential at the gyrocenter position, Φ, is related to the electrostatic potential at the particle position, ϕ, as $\Phi_{k_x,k_y} = J_0(k_\perp v_\perp/\Omega_{\mathrm{i}})\phi_{k_x,k_y}$. The zeroth-order Bessel function $J_0(k_\perp v_\perp/\Omega_{\mathrm{i}})$ represents the finite gyroradius effect. The electrostatic potential ϕ_{k_x,k_y} is calculated from the quasi-neutrality condition,

$$\int \mathrm{d}^3v J_0\delta f_{k_x,k_y} - n_0\frac{e\phi_{k_x,k_y}}{T_{\mathrm{i}}}\left[1 - \Gamma_0(b_k)\right] = n_{\mathrm{e},k_x,k_y}, \tag{6}$$

where $\delta f_{k_x,k_y}$ is the Fourier component of δf, n_0 is the average electron density, $\Gamma_0(b_k) = I_0(b_k)\exp(-b_k)$ with $b_k = (k_\perp v_{\mathrm{ti}}/\Omega_{\mathrm{i}})^2$, and I_0 is the zeroth-order modified Bessel function. The electron density perturbation n_{e,k_x,k_y} is assumed to be given in terms of the electron temperature T_{e} and the average density n_0 by

$$\frac{n_{\mathrm{e},k_x,k_y}}{n_0} = \begin{cases} e\left[\phi_{k_x,k_y} - \langle\phi_{k_x,k_y}\rangle\right]/T_{\mathrm{e}} & \text{if } k_y = 0\\ e\phi_{k_x,k_y}/T_{\mathrm{e}} & \text{if } k_y \neq 0\end{cases}. \tag{7}$$

Also, $\langle\cdots\rangle$ denotes the flux surface average.

3. Linear Simulations

To investigate ITG modes and zonal flows in LHD discharges, we perform linear simulations using the linearized version of GKV-X. We use the code to solve the Fourier transformed expression of Eq. (5) in the linear, collisionless and zero-beta case,

$$\begin{aligned}&\left(\frac{\partial}{\partial t} + v_\parallel\boldsymbol{b}\cdot\nabla - \frac{\mu}{m_{\mathrm{i}}}\boldsymbol{b}\cdot\nabla B\frac{\partial}{\partial v_\parallel} + i\omega_{\mathrm{Di}}\right)\delta f_{k_x,k_y}\\ &\quad = F_{\mathrm{M}}(-v_\parallel\boldsymbol{b}\cdot\nabla - i\omega_{\mathrm{Di}} + i\omega_{*T\mathrm{i}})J_0(k_\perp v_\perp/\Omega_{\mathrm{i}})\frac{e\phi_{k_x,k_y}}{T_{\mathrm{i}}},\end{aligned} \tag{8}$$

where ω_{Di} is the magnetic drift frequency, and $\omega_{*T\mathrm{i}}$ is the diamagnetic drift frequency with the following form:

$$\omega_{*T\mathrm{i}} = -\frac{cT_{\mathrm{i}}}{e}\frac{r_0 a}{\Psi'}k_y\left[\frac{1}{L_n} + \frac{1}{L_{T\mathrm{i}}}\left(\frac{m_{\mathrm{i}}v^2}{2T_{\mathrm{i}}} - \frac{3}{2}\right)\right]. \tag{9}$$

Here, we assume that the equilibrium radial electric field is zero. Therefore, the frequencies observed in the following simulations are regarded as those measured in the plasma frame, i.e., $\omega_{\mathrm{pl}}^{\mathrm{sim}} = \omega_{\mathrm{lab}} - \omega_{E\times B}$, if there exists an equilibrium electric field. In Eq. (9), L_n is the background gradient scale length for the density defined by $L_n^{-1} = -\mathrm{d}\ln n_{\mathrm{i}}/\mathrm{d}r$, and $L_{T\mathrm{i}}$ is the gradient scale length of the ion temperature defined by $L_{T\mathrm{i}}^{-1} = -\mathrm{d}\ln T_{\mathrm{i}}/\mathrm{d}r$. For other terms and factors in the gyrokinetic equation Eq. (8), i.e., the magnetic drift frequency, mirror force term, perpendicular wavenumber, and parallel derivative term, GKV-X employs exact forms including geometrical effects as written in Eqs. (24)-(28) in Ref. [12].

3.1 Equilibria in LHD discharges

For simulations using GKV-X, we should prepare equilibrium configurations corresponding to the experiment. In the LHD discharge of shot number 88343, the profiles of the electron density (n_{e}), ion temperature (T_{i}), and electron temperature (T_{e}) are obtained in the low-T_{i} phase ($t = 1.833$ s) and the high-T_{i} phase ($t = 2.233$ s) [10], as shown in Figs. 1-(a) and (d). Using the profiles as input to the VMEC calculation, we obtain the equilibrium field configurations corresponding to the discharge in each T_{i} phase. Hereafter, we assume $n_{\mathrm{i}}/n_{\mathrm{e}} = 1$ and $T_{\mathrm{i}}/T_{\mathrm{e}} = 1$. The radial profiles of the temperature gradient normalized by the major radius R_0, i.e., $R_0/L_{T\mathrm{i}}$, and the normalized density gradient R_0/L_n are determined from the sixth-order fitting functions of ρ for the experimental profiles of T_{i} and n_{i}, as shown in Figs. 2-(a) and (b), respectively. For the obtained equilibria, we plot the radial profiles of the safety factor in Fig. 2-(c) and the profiles along the field line of the magnetic field strength, magnetic drift frequency, and mirror force term in Figs. 3-(a), (b), and (c), respectively, where the safety factor $q = 1.7$ at $\rho = 0.61$ in the low-T_{i} phase and at $\rho = 0.65$ in the high-T_{i} phase. The field strength shown in Fig. 3-(a) for the low-T_{i} phase takes almost the same minimal value at the bottom of each helical ripple, which implies that particles trapped deep in helical ripples have very low radial drift velocities. Comparing the field strength profiles at $q = 1.7$ in Fig. 3-(a), the ripple-trapped particles are considered to have larger radial drift velocities in the high-T_{i} phase than in the low-T_{i}

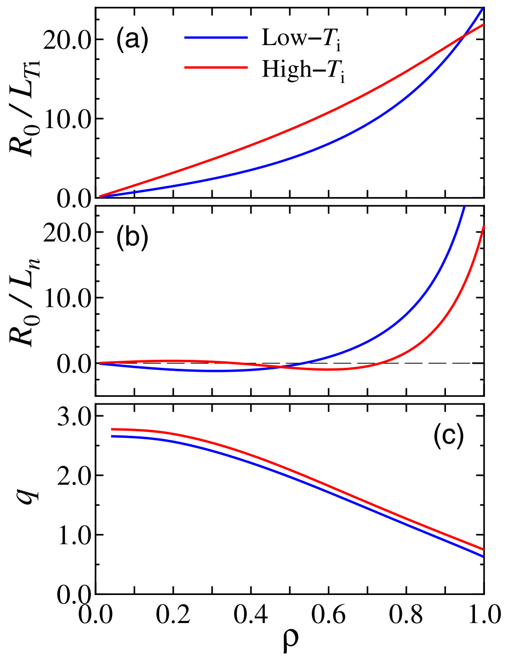

Fig. 2 Radial profiles of (a) normalized ion temperature gradient R_0/L_{Ti}, (b) normalized density gradient R_0/L_n, and (c) safety factor q in the low-T_i (blue) and high-T_i (red) phases.

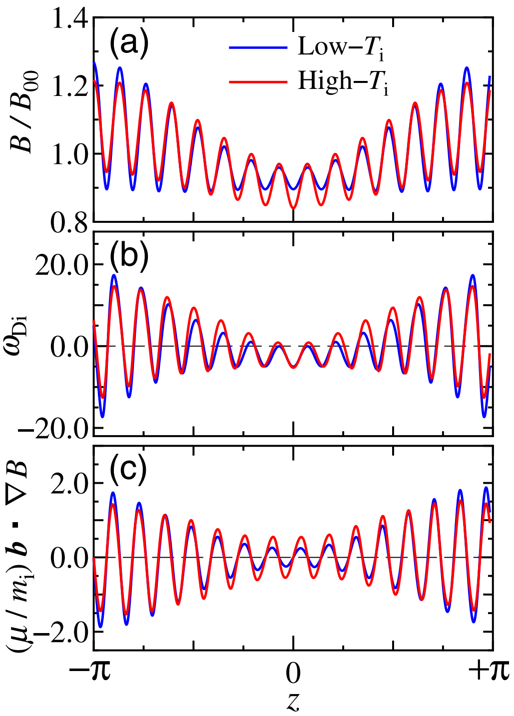

Fig. 3 Profiles along the field line for (a) normalized magnetic field strength B/B_{00}, (b) magnetic drift frequency ω_{Di} normalized by $v_{ti}R_0^{-1}/k_y\rho_{ti}$, and (c) mirror force term normalized by $(\mu B_{00}/m_i)R_0^{-1}$. All profiles are evaluated with $k_x = 0$ and $q = 1.7$ at $\rho = 0.65$ in the high-T_i phase (red) and $\rho = 0.61$ in the low-T_i phase (blue). In (b), we use $\mu/(m_i v_{ti}^2/B_{00}) = 0.71$ and $v_\parallel/v_{ti} = 1.3$.

phase. The positive and negative magnetic drift frequencies ω_{Di} represent the favorable and unfavorable magnetic curvatures for stabilization, respectively [18]. Figure 3-(b) shows that the magnetic curvature is slightly more favorable in the high-T_i phase than in the low-T_i phase.

3.2 Profiles of ITG growth rates

Figure 4 exhibits the linear growth rates and real frequencies of the ITG modes as functions of the normalized poloidal wavenumber $k_y\rho_{ti}$ in the low-T_i and high-T_i phases. The plots are evaluated with $k_x = 0$ at several radial points. The magnitudes of the growth rates and the real frequencies in the high-T_i phase are higher than those in the low-T_i phase, and the growth rates have maximum values for each radial position. For example, at $\rho = 0.65$ in the high-T_i phase, the maximum growth rate is $\gamma_{\rm max} = 0.25\ (v_{ti}/R_0)$ for $k_y\rho_{ti} = 0.35$. Therefore, we can obtain the radial profiles of the maximum growth rates as shown in Fig. 5. The unstable regions of the ITG modes are localized at the outer radial region, which agrees with the linear eigenvalue analyses [19, 20] with the modeled temperature profiles in other LHD discharges. From the plots, we can find the peaks of $\gamma_{\rm max}$ which exist at

$$\rho^{\rm sim}_{\rm peak} \sim \begin{cases} 0.83 \\ 0.65 \end{cases}, \qquad \text{and} \quad (k_y\rho_{ti})^{\rm sim}_{\rm peak} \sim \begin{cases} 0.20 & \text{for low-}T_i\text{ phase} \\ 0.35 & \text{for high-}T_i\text{ phase} \end{cases}, \tag{10}$$

in radial and wavenumber spaces, respectively. When the results are compared with the fluctuation measurements

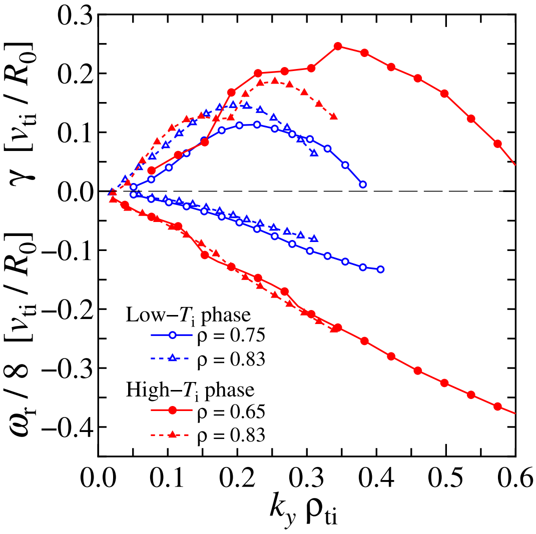

Fig. 4 Growth rates γ (top) and real frequencies ω_r (bottom) of the linear ITG modes as functions of the normalized poloidal wavenumbers $k_y\rho_{ti}$ in the low-T_i (blue) and high-T_i (red) phases. Open circles and open triangles show the results in the low-T_i phase at $\rho = 0.75$ and $\rho = 0.83$, respectively. Solid circles and solid triangles correspond to the results in the high-T_i phase at $\rho = 0.65$ and $\rho = 0.83$, respectively.

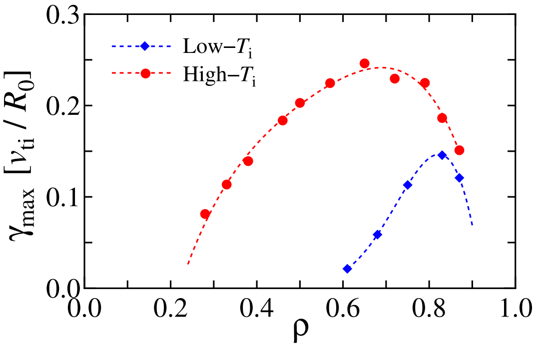

Fig. 5 Radial profiles of γ_max for the low-T_i (blue diamonds) and high-T_i (red circles) phases.

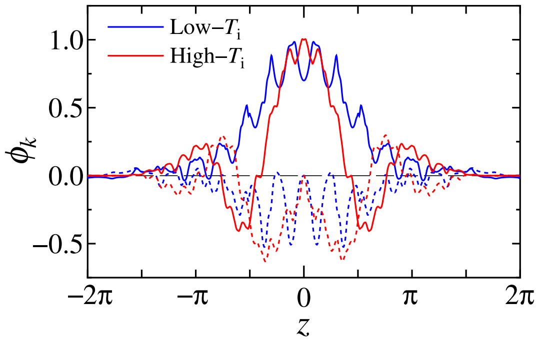

Fig. 6 Eigenfunctions of the electrostatic potentials $\phi_k = \phi_\mathrm{r} + i\phi_\mathrm{i}$ along the field line coordinate z in the low-T_i phase at $\rho = 0.83$ and $k_y\rho_\mathrm{ti} = 0.20$ (blue) and the high-T_i phase at $\rho = 0.65$ and $k_y\rho_\mathrm{ti} = 0.35$ (red). Real and imaginary parts of the eigenfunctions are plotted by solid and dotted curves, respectively.

in the LHD discharge, the regions of the density fluctuation peaks shown in Eq. (1) are located around the positions where the ITG modes are most unstable in radial and wavenumber spaces. From the real frequencies ω_r in Fig. 4, the phase velocities at $\rho = \rho^\mathrm{sim}_\mathrm{peak}$ in the plasma frame, $v^\mathrm{sim}_\mathrm{ph} = \omega_\mathrm{r}/k_y$, can also be roughly estimated as

$$v^\mathrm{sim}_\mathrm{ph} \sim \begin{cases} -2.0\times10^2\ \mathrm{m/s} & \text{for low-}T_\mathrm{i}\text{ phase} \\ -1.2\times10^3\ \mathrm{m/s} & \text{for high-}T_\mathrm{i}\text{ phase} \end{cases}. \tag{11}$$

The phase velocities are qualitatively consistent with the experimental observation that the velocity in the high-T_i phase is faster than that in the low-T_i phase, although the absolute values of the velocities are smaller than those in the experiment. Thus, considering the error bars of the experimental data, the density fluctuations observed in the LHD experiments are attributed to the ITG modes.

At $\rho = \rho^\mathrm{sim}_\mathrm{peak}$, the eigenfunctions of the electrostatic potentials $\phi_k = \phi_\mathrm{r} + i\phi_\mathrm{i}$ are also obtained as shown in Fig. 6. Both eigenfunctions have ballooning structures, which are typical of the ITG instability. Because helical ripples in the magnetic field have larger amplitudes in the outer radial region, the eigenfunctions at $\rho = 0.83$ in the low-T_i phase are more strongly corrugated than those at $\rho = 0.65$ in the high-T_i phase. In the high-T_i phase, the ITG mode has higher growth rates and more localized structure at the outside of the torus, $-\pi/2 < z < \pi/2$, than the low-T_i phase.

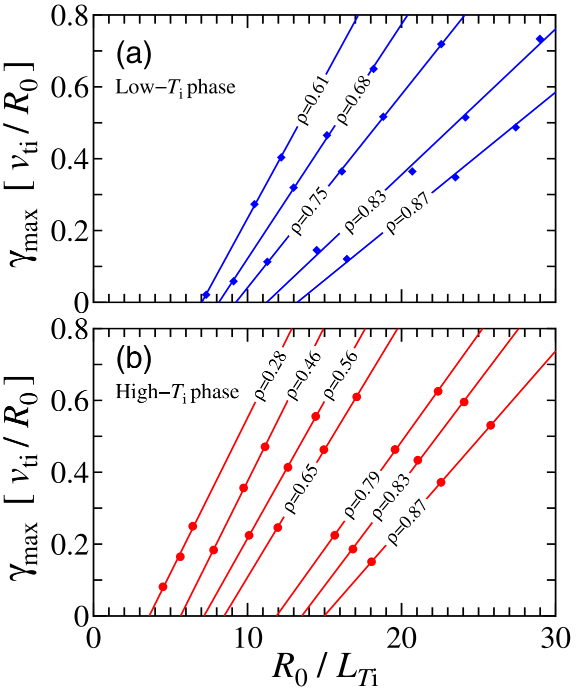

Fig. 7 $R_0/L_{T\mathrm{i}}$ dependence of γ_max at several radial positions in (a) the low-T_i phase and (b) the high-T_i phase. Lines in both plots show linear fitting functions for each radial position.

3.3 Critical ion temperature gradient

To find the critical ion temperature gradient for the ITG mode in the low- and high-T_i phases, we investigate the dependence of the ITG mode growth rates on the temperature gradient. In Fig. 7, the dependence of γ_max on the normalized ion temperature gradient $R_0/L_{T\mathrm{i}}$ is plotted with all parameters except the temperature gradient fixed at the equilibrium values for several radial positions. From the plots, we calculate the linear fitting function for each radial position and obtain the critical values of $R_0/L_{T\mathrm{i}}$ by extrapolating the fitting functions to the point where γ_max vanishes. In Fig. 8, we show the critical values for the low- and high-T_i phases as functions of ρ. Noting the deviation of the temperature gradient from the critical value in the figure, we find that the γ_max value given by Fig. 5 peaks at a radial position where the deviation is largest. The critical values are higher than the experimental values for $\rho \lesssim 0.6$ in the low-T_i phase and for $\rho \lesssim 0.2$ in the high-T_i phase, where γ_max vanishes in Fig. 5.

In the radial profiles of the critical temperature gradient, the critical values for the high-T_i phase are higher than those for the low-T_i-phase. The higher critical tem-

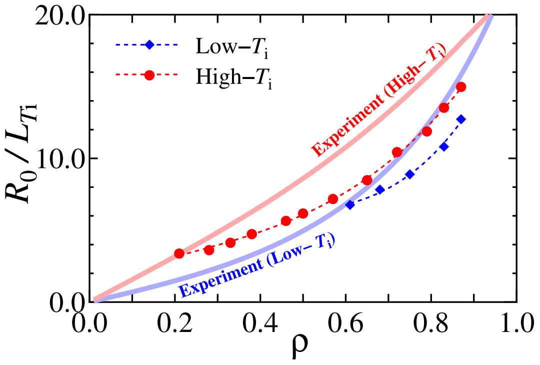

Fig. 8 Radial profiles of the critical temperature gradient in the low-T_i (blue diamonds) and high-T_i (red circles) phases. Bold curves in light blue and light red represent the experimental profiles of R_0/L_{Ti} in the low- and high-T_i phases, respectively.

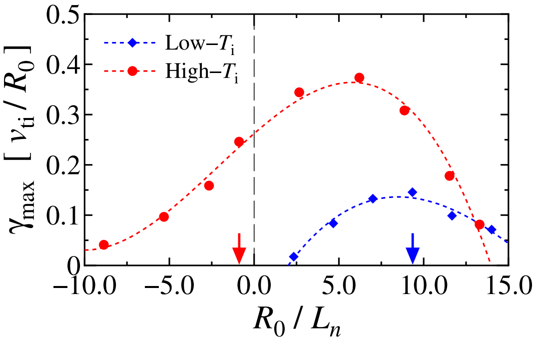

Fig. 9 R_0/L_n dependence of γ_{max} in the low-T_i phase at $\rho = 0.83$ (blue diamonds) and the high-T_i at $\rho = 0.65$ (red circles). The values of R_0/L_n from the experimental observations are represented by the blue arrow (low-T_i at $\rho = 0.83$) and red arrow (high-T_i at $\rho = 0.65$). R_0/L_{Ti} and other parameters except R_0/L_n are fixed at equilibrium values. Therefore, an increase in R_0/L_n implies an increase in the pressure gradient and a decrease in $\eta_i = L_n/L_{Ti}$.

perature gradient is considered to contribute to the plasma confinement capability. In fact, as explained by Fig. 3-(b) in Sec. 3.1, the magnetic drift frequency ω_{Di} for the high-T_i phase shifts slightly in the positive direction at around $z \sim 0$, which implies a more favorable magnetic curvature for the stabilization of the ITG mode in the high-T_i phase than in the low-T_i phase. In addition, the lower density gradients in the high-T_i phase than in the low-T_i phase are also considered to contribute to the higher critical temperature gradients in the high-T_i phase.

For the density gradient length L_n, we also perform the same analysis. Figure 9 shows the R_0/L_n dependence of γ_{max} with all parameters except R_0/L_n fixed at the equilibrium values in the low- and high-T_i phases. The plots are evaluated at $\rho = \rho^{sim}_{peak}$ in both T_i phases. In the high-T_i phase, the ITG modes are unstable for a broad range of R_0/L_n with positive and negative signs. In the figure, an increase in R_0/L_n implies an increase in the pressure gradient and a decrease in $\eta_i \equiv L_n/L_{Ti}$ because R_0/L_{Ti} is fixed. We find that the ITG mode is stabilized at $R_0/L_n \gtrsim 14$ ($\eta_i \lesssim 0.85$) for the high-T_i phase and at $R_0/L_n \gtrsim 17$ ($\eta_i \lesssim 0.82$) for the low-T_i phase. The changes in γ_{max} for the density gradient lengths at $\rho \sim \rho^{sim}_{peak} \pm 0.1$, that is, $R_0/L_n \sim 9.3 \pm 2.0$ in the low-T_i phase and $R_0/L_n \sim -0.9 \pm 0.2$ in the high-T_i phase, are within a few percent of the central values. Concluding from the R_0/L_{Ti} dependence of γ_{max} in Fig. 7, it can be stated that the effect of errors in the density gradient on the ITG growth rates is negligible, whereas changes in the ion temperature gradients greatly affect the growth rates in the LHD discharge.

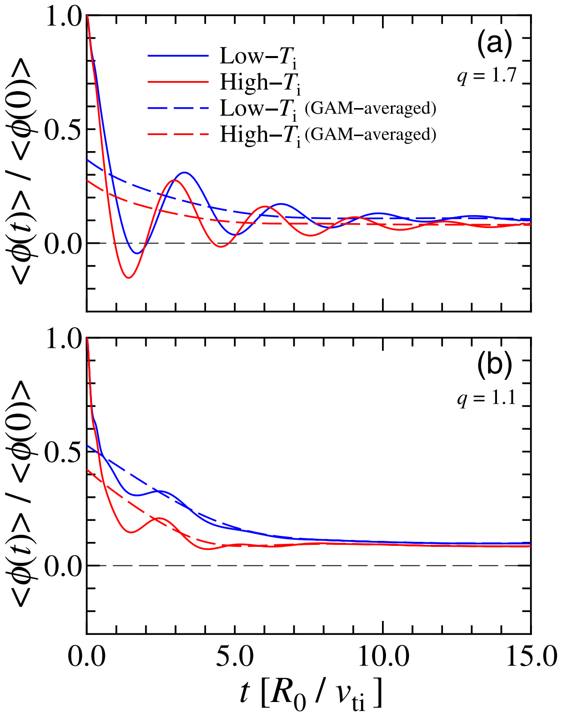

Fig. 10 Linear responses of zonal flow potentials for the radial wavenumber $k_x\rho_{ti} = 0.24$ for (a) $q = 1.7$ at $\rho = 0.61$ (low-T_i phase, solid blue curve) and at $\rho = 0.65$ (high-T_i phase, solid red curve), (b) $q = 1.1$ at $\rho = 0.83$ (low-T_i, solid blue curve) and at $\rho = 0.87$ (high-T_i, solid red curve). Dashed curves represent GAM-averaged response kernels $\mathcal{K}_L(t)$.

3.4 Zonal flow response

Zonal flows are produced by an electrostatic potential perturbation that varies in the radial direction but takes a constant value on a flux surface (hence $k_y = 0$). Therefore, the diamagnetic drift frequency ω_{*Ti} in Eq. (8) does not appear in the gyrokinetic equation for the zonal flow components. In Fig. 10, we show the response functions of the flux surface averaged zonal flow potentials to the initial perturbation, $\langle\phi_{k_\perp}(t)\rangle/\langle\phi_{k_\perp}(0)\rangle$, during their linear collisionless damping in the low- and high-T_i phases. The results are obtained for the same perpendicular wavenum-

Table 1 Comparison of residual zonal flow levels at $t \sim 23$ $(R_0/v_{\rm ti})$ in low-$T_{\rm i}$ and high-$T_{\rm i}$ phases for two safety factors, q = 1.7 and 1.1.

	q = 1.7	
	Low-$T_{\rm i}$ (ρ = 0.61)	High-$T_{\rm i}$ (ρ = 0.65)
$\mathcal{K}_{\rm L}$ ($k_x\rho_{\rm ti}$ = 0.12)	$(3.79 \pm 0.19) \times 10^{-2}$	$(3.58 \pm 0.48) \times 10^{-2}$
$\mathcal{K}_{\rm L}$ ($k_x\rho_{\rm ti}$ = 0.24)	$(8.97 \pm 0.17) \times 10^{-2}$	$(7.42 \pm 0.22) \times 10^{-2}$
	q = 1.1	
	Low-$T_{\rm i}$ (ρ = 0.83)	High-$T_{\rm i}$ (ρ = 0.87)
$\mathcal{K}_{\rm L}$ ($k_x\rho_{\rm ti}$ = 0.12)	$(3.02 \pm 0.38) \times 10^{-2}$	$(3.00 \pm 0.18) \times 10^{-2}$
$\mathcal{K}_{\rm L}$ ($k_x\rho_{\rm ti}$ = 0.24)	$(9.48 \pm 0.09) \times 10^{-2}$	$(8.33 \pm 0.20) \times 10^{-2}$

ber, $k_x\rho_{\rm i} = 0.24$, and two safety factors, $q = 1.7$ and 1.1. Radial positions are determined by the radial profiles of the safety factors in Fig. 2-(c), i.e., $\rho = 0.61$ (low-$T_{\rm i}$ phase) and $\rho = 0.65$ (high-$T_{\rm i}$ phase) for $q = 1.7$, and $\rho = 0.83$ (low-$T_{\rm i}$ phase) and $\rho = 0.87$ (high-$T_{\rm i}$ phase) for $q = 1.1$. The figures show clear contrasts between the low-$T_{\rm i}$ and high-$T_{\rm i}$ phases in the early zonal flow evolution for both safety factors. In addition, the geodesic acoustic mode (GAM) oscillations at the lower safety factor ($q = 1.1$) are damped faster than those at the higher one ($q = 1.7$). This agrees with theoretical studies [21, 22] as well as drift kinetic calculations [23].

The GAM-averaged response kernel $\mathcal{K}_{\rm L}(t)$ is defined by

$$\mathcal{K}_{\rm L}(t) = \frac{1}{\tau_{\rm GAM}} \int_{t-\tau_{\rm GAM}/2}^{t+\tau_{\rm GAM}/2} \frac{\langle \phi_{k_\perp}(t') \rangle}{\langle \phi_{k_\perp}(0) \rangle} {\rm d}t', \quad \text{for } t \geq \frac{\tau_{\rm GAM}}{2}, \tag{12}$$

where $\tau_{\rm GAM}$ is the period of the GAM oscillations. The evolution of $\mathcal{K}_{\rm L}(t)$ is shown in Fig. 11, and the residual zonal flow levels are evaluated at $t \sim 23$ $(R_0/v_{\rm ti})$, as presented in Table 1, for $k_x\rho_{\rm i} = 0.12$ and 0.24. According to an analytical study [21], the early behavior of $\mathcal{K}_{\rm L}(t)$ depends mainly on the Fourier spectrum of the field strength. In the late evolution, the residual zonal flow level is affected by the perpendicular wavenumber as well as the field spectrum. Figure 11 shows that the initial behavior of $\mathcal{K}_{\rm L}$ for $t \lesssim 1.0$ $(R_0/v_{\rm ti})$ does not change for different perpendicular wavenumbers, but is influenced by the equilibrium with the different $T_{\rm i}$ profiles for each safety factor. We also observe that the residual zonal flow levels are enhanced by increasing the radial wavenumber and are also influenced by the helical Fourier components, which depend on the radial position and the $T_{\rm i}$ profile, as seen in Fig. 3-(a). These simulation results are consistent with the analytical conclusions for the zonal flow responses [21]. Note that the neoclassical transport optimized LHD configuration, the so-called inward-shifted LHD configuration, yields a larger $\mathcal{K}_{\rm L}(t)$ than that in the standard LHD configuration [24]. In our simulations, in fact, the field strength spectrum of the low-$T_{\rm i}$ phase is similar to that of the inward-shifted LHD configuration used in Refs. [7, 24]. Hence $\mathcal{K}_{\rm L}(t)$ is larger in the low-$T_{\rm i}$ phase than in the high-$T_{\rm i}$ phase.

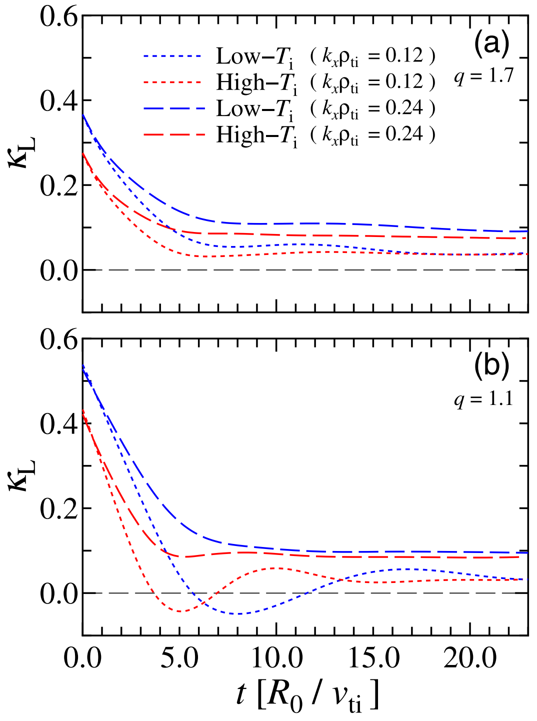

Fig. 11 Evolutions of the GAM-averaged response kernels $\mathcal{K}_{\rm L}(t)$ for $k_x\rho_{\rm ti} = 0.12$ (dotted curves) and $k_x\rho_{\rm ti} = 0.24$ (dashed curves) for (a) $q = 1.7$ and (b) $q = 1.1$ at the same radial positions as in Fig. 10. Blue and red curves represent the results for the low-$T_{\rm i}$ and high-$T_{\rm i}$ phases, respectively.

4. Conclusions

In this study, we investigated ITG modes and zonal flows in LHD discharges by using linear gyrokinetic simulations. We focused on the high-ion-temperature LHD discharge where the density fluctuations are measured in radial, wavenumber, and phase velocity spaces. In the simulations of the low- and high-$T_{\rm i}$ phases in the discharge, the unstable ITG modes with typical ballooning structures have growth rates that peak at radial positions with the largest deviation of the temperature gradient from the critical values. The peak positions of the growth rate in radial and wavenumber spaces are close to the regions where density fluctuation peaks are measured experimentally. The critical temperature gradients in the high-T_i phase are higher than those in the low-T_i phase. The former phase has more favorable magnetic curvature and lower density gradients than the latter. In addition, the characteristics of the phase velocities of the ITG modes agree qualitatively with the experimental observations. From the simulation results, therefore, the experimentally observed increases in the fluctuations are attributed to ITG instability. On the other hand, we observed that the Fourier spectra of the field strength affect the early behavior of the zonal flow responses in different T_i phases, whereas the residual levels are influenced by the radial wavenumber, the radial position, and the field spectra, as predicted theoretically.

ITG turbulence is considered to play a vital role in anomalous ion heat transport in low-β plasmas. Nonlinear gyrokinetic ITG turbulence simulations are required to quantitatively evaluate the amplitudes and spectra of the turbulent fluctuations and the resulting anomalous transport coefficients. Although the present analyses are limited to linear simulations of the ITG modes and zonal flows, nonlinear simulations of ITG turbulence under the LHD's experimental conditions are currently in progress as the next step of this study, and the results will be reported elsewhere.

Acknowledgments

One of the authors (M.N.) thanks Prof. K.Y. Watanabe for providing useful information on equilibrium calculation in the LHD experiments. This work is supported in part by the Japanese Ministry of Education, Culture, Sports, Science and Technology, Grants No. 22760660 and 21560861, and in part by the NIFS Collaborative Research Program, NIFS09KTAL022, NIFS10KDAT020, and NIFS10KNXN186.

[1] W. Horton, Rev. Mod. Phys. **71**, 735 (1999).

[2] O. Motojima, N. Ohyabu, A. Komori *et al.*, Nucl. Fusion **43**, 1674 (2003).

[3] O. Kaneko, M. Yokoyama, M. Yoshinuma *et al.*, Plasma Fusion Res. **4**, 027 (2009).

[4] P.H. Diamond, S.-I. Itoh, K. Itoh and T.S. Hahm, Plasma Phys. Control. Fusion **47**, R35 (2005).

[5] K. Itoh, S.-I. Itoh, P.H. Diamond and A. Fujisawa, Phys. Plasmas **13**, 055502 (2006).

[6] A. Fujisawa, Nucl. Fusion **49**, 013001 (2009).

[7] T.-H. Watanabe, H. Sugama and S. Ferrando-Margalet, Phys. Rev. Lett. **100**, 195002 (2008).

[8] H. Sugama, T.-H. Watanabe and S. Ferrando-Margalet, Plasma Fusion Res. **3**, 041 (2008).

[9] K. Ida, M. Yoshinuma, M. Osakabe *et al.*, Phys. Plasmas **16**, 056111 (2009).

[10] K. Tanaka, C.A. Michael, L.N. Vyacheslavov *et al.*, Plasma Fusion Res. **5**, S2053 (2010).

[11] K. Tanaka, C.A. Michael, L.N. Vyacheslavov *et al.*, Rev. Sci. Instrum. **79**, 10E702 (2008).

[12] M. Nunami, T.-H. Watanabe and H. Sugama, Plasma Fusion Res. **5**, 016 (2010).

[13] S.P. Hirshman and O. Betancourt, J. Comput. Phys. **96**, 99 (1991).

[14] A.H. Boozer, Phys. Fluids **11**, 904 (1980).

[15] M.A. Beer, S.C. Cowley and G.W. Hammett, Phys. Plasmas **2**, 2687 (1995).

[16] T.-H. Watanabe and H. Sugama, Nucl. Fusion **46**, 24 (2006).

[17] E.A. Frieman and L. Chen, Phys. Fluids **25**, 502 (1982).

[18] T. Kuroda and H. Sugama, J. Phys. Soc. Jpn. **70**, 2235 (2001).

[19] O. Yamagishi, M. Yokoyama, N. Nakajima and K. Tanaka, Phys. Plasmas **14**, 012505 (2007).

[20] G. Rewoldt, L.-P. Ku, W.M. Tang *et al.*, Nucl. Fusion **42**, 1047 (2002).

[21] H. Sugama and T.-H. Watanabe, Phys. Plasmas **13**, 012501 (2006).

[22] S.V. Novakovskii, C.S. Liu, R.Z. Sagdeev and M.N. Rosenbluth, Phys. Plasmas **4**, 4272 (1997).

[23] S. Satake, H. Sugama and T.-H. Watanabe, Nucl. Fusion **47**, 1258 (2007).

[24] S. Ferrando-Margalet, H. Sugama and T.-H. Watanabe, Phys. Plasmas **14**, 122505 (2007).